Evolution of Metallicity in Vanadium Dioxide by Creation of Oxygen Vacancies

Zhen Zhang,[1] Fan Zuo,[1] Chenghao Wan,[2] Aveek Dutta,[3] Jongbum Kim,[3] Jura Rensberg,[4] Ronny Nawrodt,[4] Helen Hejin Park,[5,9] Thomas J. Larrabee,[5,8] Xiaofei Guan,[6] You Zhou,[7] S. M. Prokes,[5] Carsten Ronning,[4] Vladimir M. Shalaev,[3] Alexandra Boltasseva,[3] Mikhail A. Kats,[2] and Shriram Ramanathan[1,*]

[1]*School of Materials Engineering, Purdue University, West Lafayette, Indiana 47907, USA*
[2]*Department of Electrical and Computer Engineering, Department of Materials Science and Engineering, University of Wisconsin-Madison, Madison, Wisconsin 53706, USA*
[3]*School of Electrical and Computer Engineering and Birck Nanotechnology Center, Purdue University, West Lafayette, Indiana 47907, USA*
[4]*Institute for Solid State Physics, Friedrich Schiller University Jena, 07743 Jena, Germany*
[5]*United States Naval Research Laboratory, Washington, D.C. 20375, USA*
[6]*John A. Paulson School of Engineering and Applied Sciences, Harvard University, Cambridge, Massachusetts 02138, USA*
[7]*Department of Chemistry and Chemical Biology, Harvard University, Cambridge, Massachusetts 02138, USA*
[8]*National Research Council Research Associate at the Naval Research Laboratory, Washington, D.C. 20375, USA*
[9]*American Society for Engineering Education Research Associate at the Naval Research Laboratory, Washington, D.C. 20375, USA*

(Received 2 November 2016; published 10 March 2017)

Tuning of the electronic state of correlated materials is key to their eventual use in advanced electronics and photonics. The prototypical correlated oxide (VO_2) is insulating at room temperature and transforms to a metallic state when heated to 67 °C (340 K). We report the emergence of a metallic state that is preserved down to 1.8 K by annealing thin films of VO_2 at an ultralow oxygen partial pressure ($P_{O_2} \sim 10^{-24}$ atm). The films can be reverted back to their original state by annealing in oxygen, and this process can be iterated multiple times. The metallic phase created by oxygen deficiency has a tetragonal rutile structure and contains a large number of oxygen vacancies far beyond the solubility at equilibrium (greater than approximately 50 times). The oxygen starvation reduces the oxidation state of vanadium from V^{4+} to V^{3+} and leads to the metallization. The extent of resistance reduction (concurrent with tuning of optical properties) can be controlled by the time-temperature envelope of the annealing conditions since the process is diffusionally driven. This experimental platform, which can extensively tune oxygen vacancies in correlated oxides, provides an approach to study emergent phases and defect-mediated adaptive electronic and structural phase boundary crossovers.

DOI: 10.1103/PhysRevApplied.7.034008

I. INTRODUCTION

Point defects and disorder strongly influence the properties of correlated electron materials [1,2]. The electronic properties of the ground state can be perturbed by several mechanisms arising from disorder, including electron donation into the conduction band from charged defects [3], and aliovalent substitutional doping and related effects [4–6]. Vanadium dioxide (VO_2) is a well-known phase-change material that is studied for various applications in electronics and photonics [7–10]. It is a prototypical correlated oxide system that possesses a monoclinic insulating state at room temperature and transforms to a metallic state with a tetragonal rutile structure when heated past approximately 67 °C [11–13]. The insulating state of VO_2 at room temperature is a result of a combination of Mott and Peierls mechanisms, where the electron-electron correlations and electron-lattice-coupled dimerization of vanadium ions lead to the opening of an energy gap [11,12,14–19]. As a result, the metal-insulator transition is very sensitive to disorder, which can alter the correlation effects [20–22]. Ion-irradiation experiments have shown how site disorder can modulate the metal-insulator transition [8,23]. Substitutional defects such as W or Mo dopants, as well as interstitial defects such as hydrogen, can also dramatically modify the phase-transition temperature and even stabilize the metallic phase down to a few kelvin [4,6,20,24]. However, these modifications are either irreversible (e.g., Mo and W dopants) [4,6] or require catalytic electrodes coated on the surface [20].

While studies dating back over four decades have been carried out on chemical doping of VO_2, a recent topic of

*Shriram@purdue.edu

great interest is the emergence of metallic phases and large reversible resistance modulation in electric double-layer thin-film transistors [25–31]. The ground-state resistance of VO_2 thin films is modulated by creating oxygen deficiency via electrochemical reactions between the VO_2 and the ionic liquid electrolyte [26,28]. Such a metallic state is nonvolatile and potentially enables applications in memory electronics, photonics, and optical metamaterials [8,26,31]. However, creation of oxygen deficiency by ionic liquid gating is possibly linked with both hydrogen intercalation whence a trace of water remains in ionic liquid [29] and degradation of the entire film under high electric field [28].

Other than electrolyte gating with an ionic liquid, very few methods exist to create sufficient oxygen deficiency to fully suppress the metal-insulator transition of VO_2 in a reversible manner. Perhaps the simplest way to introduce oxygen deficiency in VO_2 films is to reduce the oxygen content during high-temperature synthesis [32,33]. For phase-pure oxygen-deficient $VO_{2-\delta}$ (δ is the value of oxygen deficiency) thin films, a suppression of the metal-insulator-transition temperature has been observed by about 15 °C [32]. However, further reducing the oxygen content during high-temperature synthesis encounters the formation of Magnéli phases V_nO_{2n-1} ($3 \leq n \leq 8$) [32,34] with lower oxygen stoichiometric ratios than VO_2 [35], which then prevents the creation of oxygen deficiency in VO_2 within a single phase over a broad range. Low-temperature (450 °C) with low-vacuum (30 mTorr) annealing is another approach to introduce oxygen deficiency and prevent the formation of Magnéli phases [36]; however, in those studies, complete suppression of the metal-insulator transition was not observed. As a result, it is still a topic of active study whether or not disorder in anion sublattices (e.g., oxygen vacancies) solely can disturb and fully suppress the metal-insulator transition of vanadium dioxide.

Here we demonstrate a reversible metallization of VO_2 that does not require high-field ionic liquid gating or the use of hydrogen or protons as a dopant. Our approach uses low-temperature annealing at an ultralow oxygen partial pressure ($P_{O_2} \sim 10^{-24}$ atm). This environment is created by a dry-oxygen-gettering technique that does not rely on mixing hydrogen, water, or carbon monoxide gases, and is generally challenging to achieve in a film growth chamber. The resulting metallic state is stable down to 1.8 K, and the samples can be recovered back to their original state by annealing in oxygen at elevated temperature. We find that the emergence of the metallic state is accompanied by a substantial increase of reflectance in the mid-infrared-wavelength range. In addition, the metallized state possesses a tetragonal rutile structure with an oxygen-deficiency level of $VO_{2-\delta}$, $\delta \sim 0.2$, far beyond its solubility in equilibrium ($\delta \sim 0.004$) [35]. The metallization of VO_2 results from the reduction of vanadium ions from V^{4+} to V^{3+} when oxygen vacancies are introduced.

II. EXPERIMENT

A. Experimental setup to create low-oxygen-pressure environment and metallization of VO_2

The experimental setup for generating low oxygen partial pressures is shown in Fig. 1(a). Ultra-high-purity (UHP) argon (Ar) is utilized as the starting gas and is then filtered with a Mg-based oxygen trap (Appendix A) with a flow rate of 50 ml/ min. When UHP Ar flows into the oxygen trap, the trace amount of O_2 reacts with the hot Mg (approximately 450 °C) following the reaction: $2Mg + O_2(g) = 2MgO$. The MgO formed through this process is porous and, thus, does not prevent further reactions from taking place. As shown in Fig. 1(b), when the oxygen trap is on, the oxygen partial pressure of the annealing system drops quickly and can reach approximately 10^{-24} atm. The oxygen partial pressure in the annealing system is monitored using zirconia-based oxygen sensors (Appendix B). To prevent O_2 contamination from the outside, a water trap is utilized at the end port of the annealing chamber. We do not need to mix hydrogen or carbon-containing gases or fabricate electrodes or devices to achieve oxygen depletion in VO_2 films, so it is a clean way to study electronic and optical properties of oxides under oxygen deprivation.

The oxygen deprivation of VO_2 (deposited on sapphire substrate) in the annealing chamber is schematically shown in Fig. 1(c). During annealing, the sapphire substrate remains stable (see Supplemental Material 1 [37]), which enables us to study the evolution of oxide films. At low oxygen partial pressure, the VO_2 phase becomes less stable than the Magnéli phases, which possess lower oxygen stoichiometric ratios (see Supplemental Material 2 [37]). In our work, the VO_2 is held at low annealing temperatures (≤400 °C) where the structural transformation to Magnéli phases is hindered kinetically (see Supplemental Material 2 [37]). The combination of low oxygen partial pressure and low annealing temperature, thus, enables the formation of oxygen vacancies in tetragonal VO_2 [Fig. 1(c)]. The electrons generated via the oxygen deprivation reduce the vanadium ions from V^{4+} to V^{3+}. The principal chemical reactions that occur at the low oxygen partial pressure are

$$O_o^x \leftrightarrow v_O^{2+} + 2e^- + \frac{1}{2}O_2(g), \tag{1}$$

$$V^{4+} + e^- \leftrightarrow V^{3+}, \tag{2}$$

where O_o^x stands for the oxygen normally occupied at the anion site, v_O^{2+} stands for oxygen vacancies, and V^{4+} and V^{3+} stand for vanadium ions in the pristine and oxygen-deficient state, respectively.

The appearance of V^{3+} in the system weakens the strong electron correlation and enables the nonvolatile transformation from the insulating monoclinic phase to the metallic tetragonal phase, leading to metallization of the sample

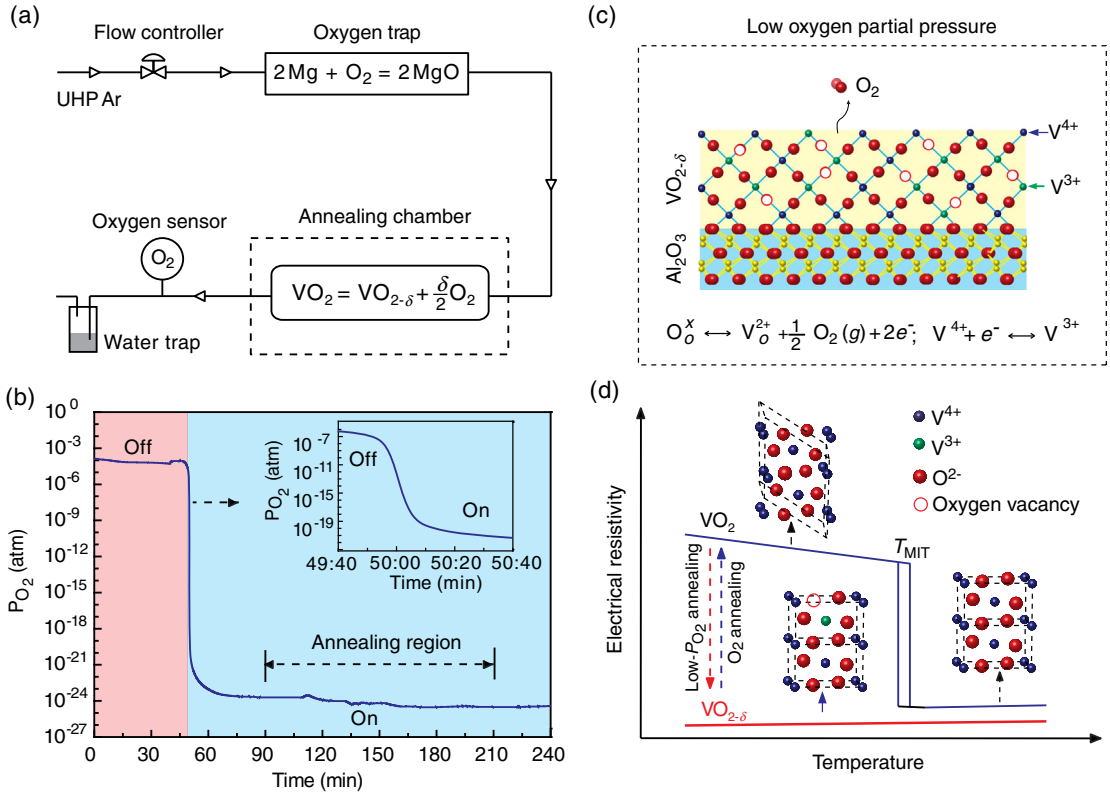

FIG. 1. Metallization of vanadium dioxide at extremely low oxygen partial pressure. (a) Experimental setup for annealing VO_2 at low oxygen partial pressure. (b) Real-time oxygen partial pressure monitored by a zirconia-based oxygen sensor, where pristine VO_2 is annealed at $P_{O_2} \sim 10^{-24}$ atm. The inset shows the P_{O_2} in a narrow time window. (c) At low oxygen partial pressure, oxygen vacancies are created in VO_2, and the oxidization state of vanadium is reduced from V^{4+} to V^{3+}. (d) By introducing a high concentration of oxygen vacancies, the metal-insulator transition is suppressed and a metallic nonvolatile $VO_{2-\delta}$ state is observed down to very low temperatures. The process can be reversed by oxygen annealing.

down to cryogenic temperatures, as shown in Fig. 1(d). It is reminiscent of the stabilization of the metallic state by introducing V^{3+} ions with Mo and W doping [4,6].

Reversal to the insulating state can be achieved by annealing the sample in an oxygen-rich environment (e.g., pure oxygen) at elevated temperature, restoring the V^{4+} oxidization state. The sample then shows the metal-insulator transition similar to the pristine samples.

B. Synthesis of VO_2 thin films

VO_2 thin films with thickness of approximately 40 nm are grown by physical vapor deposition (PVD). A V_2O_5 target is magnetron sputtered in an Ar atmosphere on *c*-plane sapphire substrates. The substrates are cleaned with acetone and isopropanol, blow dried with Ar gas, and then transferred into the growth chamber. The base pressure of the growth chamber is kept at 8×10^{-8} Torr before deposition. During deposition, the Ar flux is set to 50 sccm with the pressure of the growth chamber at 5 mTorr. The substrate is heated to 600 °C for the formation of the VO_2 phase. The target power is set as 100 W so that the growth rate is 0.7 nm/ min. The thin films are quenched to room temperature after deposition under an Ar flux of 50 sccm at 5 mTorr and then transferred out of the deposition system.

Comparable VO_2 thin films with thickness of approximately 40 nm are grown by atomic layer deposition (ALD) on *c*-plane sapphire substrate. These samples are used primarily for the annealing experiments to study the general nature of the phase-transition suppression in vanadium dioxide by oxygen deficiency independent of the specific growth technique. ALD VO_2 films are grown by a commercial Beneq TFS 200 reactor at 150 °C. The precursors for the vanadium and oxygen sources are tetrakis (ethylmethylamino)vanadium [TEMAV, $V(NEtMe)_4$, Air Liquide] and deionized H_2O, respectively, and UHP argon is used as the carrier gas. The vanadium precursor is evaporated at 60 °C from an open boat inside a hot cell attached to the reactor chamber. The exposures times for each dose of TEMAV and H_2O are 2 and 0.2 s, respectively, using an ALD sequence of TEMAV dose, UHP Ar purge, H_2O, then UHP Ar purge. VO_2 films grown by ALD are annealed in N_2 gas for approximately 1 h at 480 °C with a constant pressure of approximately 8 Torr to convert from amorphous to crystalline VO_2.

C. Structural, electrical, and optical characterization

Electrical resistivity is measured with a Keithley 2635A source meter in a temperature-controlled probe station. Low-temperature-resistivity measurements are conducted under electrical-transport mode in the Physical Property Measurement System from Quantum Design. The temperature-dependent reflectance is investigated by near-normal-incidence measurements using a mid-infrared Fourier transform infrared (FTIR) spectrometer (Bruker Vertex 70) coupled to a mid-infrared microscope (Hyperion). The reflected light is detected with a mercury cadmium telluride detector in the temperature range between 25 °C and 100 °C. The crystal structure and lattice constant are studied by high-resolution x-ray diffraction (XRD) using the PANalytical MRD X'Pert Pro. X-ray photoelectron spectroscopic (XPS) analyses are carried out to investigate the changes of the oxidation state of vanadium as well as to estimate the stoichiometry of the samples [38]. High-resolution XPS data are obtained with monochromatic x-ray (Al $K\alpha$) in vacuum of approximately 10^{-8} Torr. The XPS spectrum is calibrated with the C1s peak. Raman spectra are measured at room temperature using 532-nm excitation with a power of 1 mW in a backscattering geometry (Renishaw inVia confocal Raman microscope). The visible and near-infrared optical properties of $VO_{2-\delta}$ are studied by variable-angle spectroscopic ellipsometry (V-VASE, J. A. Woollam). The ellipsometry measurements are performed at three incident angles (55°, 65°, and 75°) at 25 °C and 90 °C, for free-space wavelengths from 200 to 2000 nm. Complex optical refractive-index values are extracted by fitting the experimental results with a thin-film model that includes the sapphire substrate, a VO_2 layer, and surface roughness (see Supplemental Material 3 [37]). In our model, the optical constants of VO_2 are described by a general oscillator function, which includes four Gaussian terms [39] for the insulator phase (found in pristine VO_2 at 25 °C) and one additional Drude term [40] for the metallic phase (found in pristine VO_2 at 90 °C and oxygen-deficient $VO_{2-\delta}$ at both 25 °C and 90 °C). For each of the films, we fit the thickness and optical constants assuming that the thickness does not change significantly as a function of the temperature.

III. RESULTS AND DISCUSSION

A. Evolution of the metallic phase

PVD-grown VO_2 films with thickness of 40 nm are annealed at low oxygen partial pressure. The electrical resistivity of VO_2 after annealing is shown in Fig. 2(a). Pristine VO_2 shows a metal-insulator transition at $T_{MIT} \sim$ 67 °C with a 3 orders of magnitude jump of electrical resistivity. The transport gap (E_g) in the insulating state estimated from fitting the temperature-dependent resistivity with the equation $\rho \sim \exp(E_g/2k_BT)$ [41] is 0.58 eV, consistent with the literature (approximately 0.6 eV)

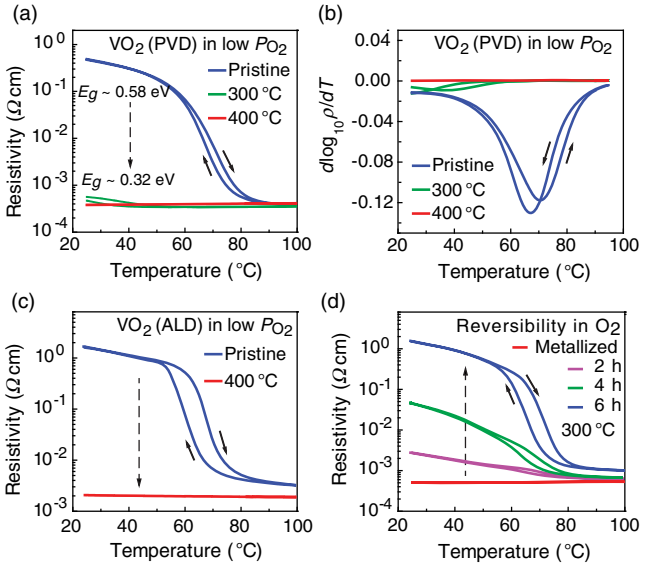

FIG. 2. Manipulation of electrical properties of VO_2 thin films after annealing at $P_{O_2} \sim 10^{-24}$ atm. (a) Resistivity-temperature curves of 40-nm PVD-grown VO_2 annealed at 300 °C and 400 °C, respectively, for 2 h. After annealing, the thin films show metallic behavior down to room temperature. (b) Corresponding derivative of the resistivity-temperature curve for various annealing conditions. (c) Resistivity-temperature curves of 40-nm ALD-grown VO_2 annealed at 400 °C for 2 h. The metallization behavior of VO_2 under low oxygen partial pressure is reproducible with ALD-grown films. (d) After metallization of 40-nm PVD-grown VO_2 at low P_{O_2} for 400 °C 2 h in (a), the sample is further annealed in pure oxygen at 300 °C for 2, 4, and 6 h. The resistivity-temperature curves show that the metal-insulator transition is recovered after annealing in oxygen.

[41]. After annealing the pristine sample at 300 °C for 2 h, the high-temperature electrical resistivity of the sample at 100 °C is found to be similar to that of pristine VO_2. However, with cooling, the sharp metal-insulator transition near 67 °C vanishes. Instead, the metal-insulator transition is suppressed to approximately 30 °C, with only a small resistivity change of approximately 2 times. The reduction of the transition temperature and the resistivity jump can be observed more clearly by taking the derivative of the resistivity with respect to the temperature, as shown in Fig. 2(b). The transport gap of the insulating state of the (300 °C)-annealed sample is reduced to 0.32 eV [Fig. 2(a)]. Such a reduction is also observed in hydrogenated VO_2 prior to the full stabilization of the metallic state [20]. The extent of the resistance reduction at low oxygen partial pressure can be controlled by varying the annealing conditions and film thickness (see Supplemental Material 4 [37]). We achieve full stabilization of the metallic state by annealing the pristine VO_2 at 400 °C for 2 h at low oxygen partial pressure. The sample retains the low electrical resistivity comparable to that of the metallic state of the pristine sample down to room temperature.

The generality of metallization of VO_2 after annealing at low oxygen partial pressure is investigated by performing annealing experiments on VO_2 thin films with similar thickness (40 nm), synthesized by ALD. The electrical resistivity of ALD-grown VO_2 after annealing at 400 °C for 2 h is shown in Fig. 2(c). Similar to the PVD case, the metal-insulator transition of VO_2 is suppressed after annealing, leaving only the metallic state. This demonstrates that the oxygen-vacancy-mediated metallic phase evolution process is independent of the growth technique.

The metallic state of VO_2 after annealing at low oxygen partial pressure can be preserved for extended periods of time in ambient condition, which indicates potential relevance to practical applications (see Supplemental Material 5 [37]). It is possible due to the kinetic limitation of oxygen diffusion into the whole film at low temperature. Since a large amount of oxygen vacancies is introduced, the $VO_{2-\delta}$ is metastable after low oxygen partial pressure annealing.

The reversibility of the metallized samples to the insulating state is studied by annealing in pure oxygen gas ($P_{O_2} \sim 1$ atm) at elevated temperatures. We start from the metallized sample obtained by annealing the 40-nm PVD-grown VO_2 at 400 °C for 2 h. This sample is then held at 300 °C in O_2 for 2, 4, and 6 h. As Fig. 2(d) shows, the low-temperature electrical resistivity of the sample gradually increases with increasing annealing duration, and the metal-insulator transition is restored. After holding the metallized sample in O_2 for 6 h at 300 °C, its transition temperature and resistivity value become similar to those of the pristine samples [Fig. 2(a)]. Moreover, the metallization of VO_2 at low oxygen partial pressure and the recovery back to the insulating state can be performed over multiple cycles (see Supplemental Material 6 [37]). The reversibility of the metallized samples under pure oxygen further suggests the oxygen deficiency created in VO_2 at low oxygen partial pressure is relevant to the emergence of the metallic state, in accordance with electrolyte gating experiments.

B. Mid-IR reflectance of the metallic phase

To investigate the effect of low oxygen partial pressure annealing on the optical properties of VO_2, mid-IR reflectance of pristine and annealed (400 °C, 2 h) samples are studied. The temperature-dependent mid-IR reflectance of pristine VO_2 during heating is shown in Fig. 3(a). At room temperature (25 °C), the pristine VO_2 is in the insulating state and is relatively transparent in the mid-IR region. The increase of reflectance above 11 μm results from the onset of the reststrahlen band of the sapphire substrate [8,42]. With increasing temperature, the reflectance increases between 2 and 10 μm, due to the increase of carrier density across the thermally induced metal-insulator transition. Around the transition temperature, a sharp increase of reflectance can be observed in Fig. 3(c).

After annealing at 400 °C for 2 h, the temperature-dependent reflectance spectrum of sample changes [Figs. 3(a) vs 3(b)]. The sample becomes highly reflective in the mid-IR region, even at room temperature, indicating a high carrier density after annealing. Upon heating, the reflectance of the annealed sample maintains a high value, and no signature of a metal-insulator transition is observed. Moreover, the reflectance of the sample decreases slightly with heating [Fig. 3(c)], demonstrating a Drude-like metallic behavior [43]. Therefore, the mid-IR reflectance of the annealed sample demonstrates that the

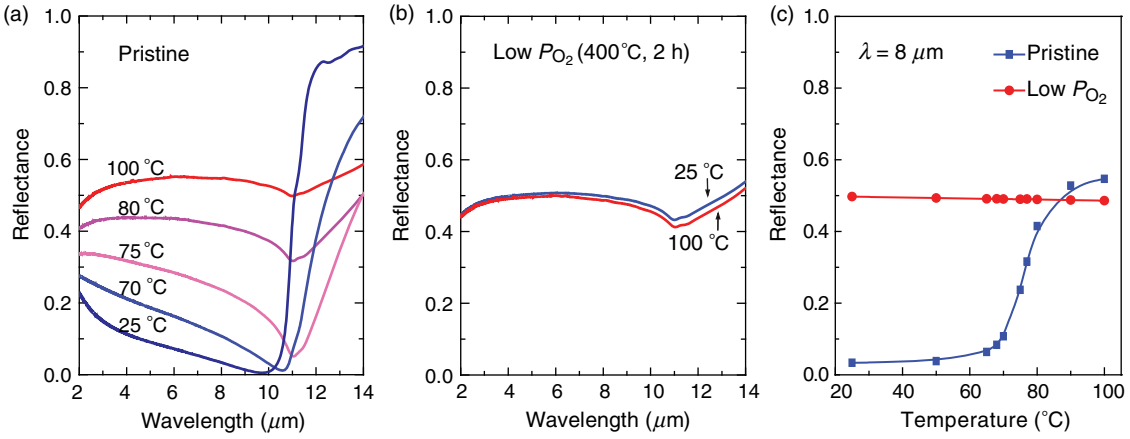

FIG. 3. Mid-IR reflectance of VO_2 before and after annealing at $P_{O_2} \sim 10^{-24}$ atm. (a) Temperature-dependent reflectance spectrum of pristine VO_2 deposited on a sapphire substrate. After annealing at $P_{O_2} \sim 10^{-24}$ atm at 400 °C for 2 h, the reflectance spectrum of the sample is shown in (b), where weak temperature-dependent behavior is observed. The sample maintains a high reflectance when cooled, demonstrating the vanishing of metal-insulator transition after annealing. (c) Single-wavelength ($\lambda = 8$ μm) temperature-dependent reflectance of VO_2 after annealing at low oxygen partial pressure at 400 °C for 2 h. The reflectance of the pristine sample increases sharply when heated past the metal-insulator-transition temperature. After annealing at low oxygen partial pressure, the sample shows high reflectance, similar to that of the thermally induced metallic state of the pristine sample. Moreover, the reflectance of the annealed sample decreases slightly with heating, indicative of metallic behavior.

metallic state is stabilized after annealing at low oxygen partial pressure. The comparison of reflectance between the annealed sample and the pristine one above T_{MIT} [Fig. 3(c)] indicates the optical similarities in the mid-IR region between the metallic states induced by temperature and oxygen deficiency.

C. Stabilization of oxygen-deficient rutile $VO_{2-\delta}$

The crystallographic properties of the metallic phase after annealing at low oxygen partial pressure are studied. The room-temperature XRD profiles of pristine PVD-grown 40-nm VO_2 before and after annealing at 400 °C for 2 h are shown in Figs. 4(a) and 4(b). For the pristine VO_2 thin film, $(020)_M$ and $(040)_M$ (M stands for monoclinic) diffraction peaks are observed indicating its epitaxial growth with orientation relation VO_2 (020) aligning with Al_2O_3 (0006) [44]. After annealing, as Fig. 4(b) shows, the $(020)_M$ peak shifts to a lower diffraction angle with $2\theta = 39.4°$, which is very close to the diffraction peak from the (200) plane of the tetragonal rutile structure ($2\theta = 39.5°$) [45]. This shifting is similar to that of the thermally induced transformation from monoclinic to tetragonal rutile structure in VO_2. Except for the peak shifting, no new diffraction peak appears, indicating that the metallization of the thin film is not caused by the structural transformation from VO_2 to any of the Magnéli phases. Moreover, we confirm the tetragonal rutile structure of the metallized sample by observing an off-axis (220) diffraction spot at tilting angle $\psi = 45°$ (see Supplemental Material 7 [37]). The lattice parameter of the metallized sample at room temperature is extracted from the off-axis diffraction scans as $a = b = 4.56$ Å; $c = 2.86$ Å, close to that of the pristine VO_2 in the high-temperature rutile phase ($a = b = 4.55$ Å; $c = 2.85$ Å) [45].

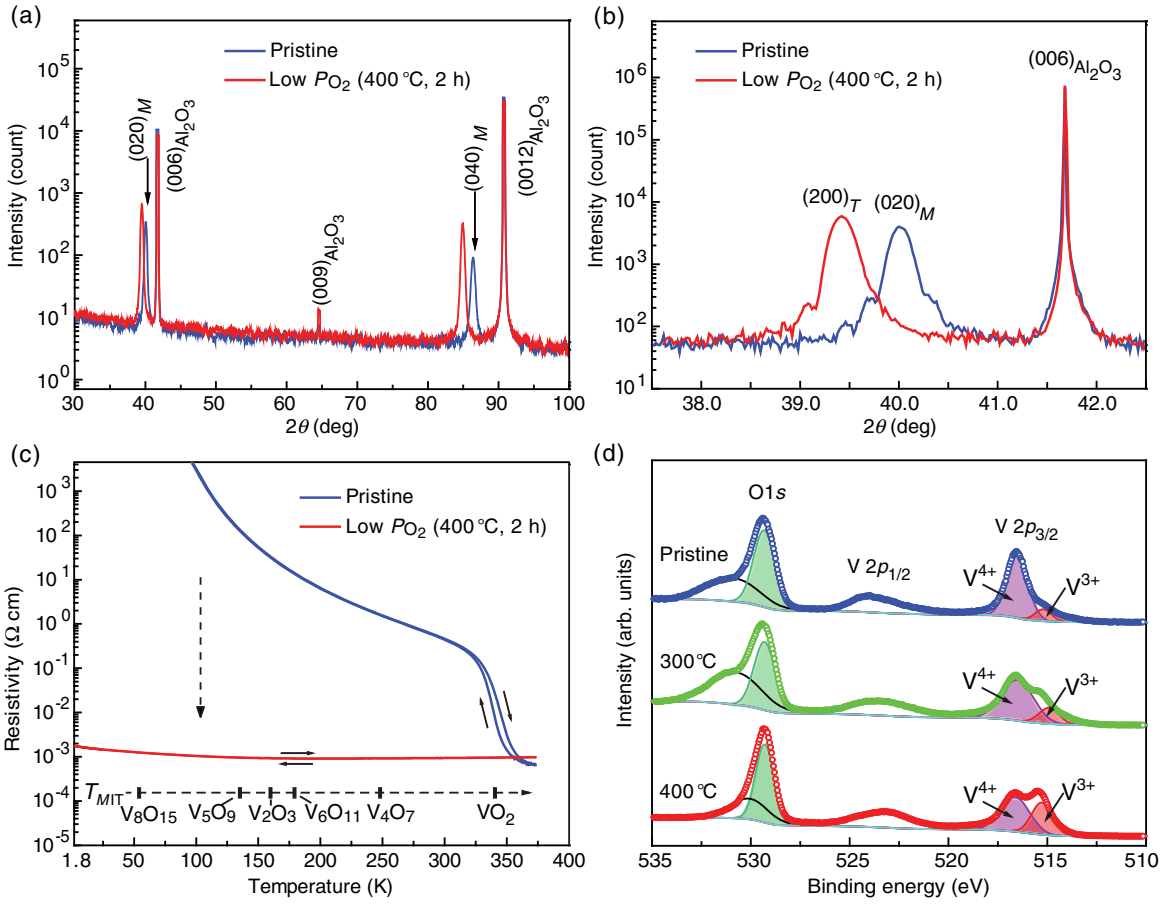

FIG. 4. XRD curves of pristine and annealed VO_2 thin films (a) over a wide range of angles and (b) around the $(020)_M$ peak. The shifting of the $(020)_M$ peak to the $(200)_T$ peak demonstrates that the high-temperature tetragonal (rutile) structure is maintained down to room temperature after annealing. (c) The resistivity of annealed thin films is measured down to 1.8 K. The metal-insulator-transition temperatures of various Magnéli phases are depicted. The flat resistivity-temperature curve over the entire temperature range indicates the absence of Magnéli phases in the oxygen-deficient $VO_{2-\delta}$ thin films. (d) XPS analysis of pristine and annealed thin films. The shifting of $V2p_{1/2}$ to lower binding energy and the appearance of $V^{3+}2p_{3/2}$ photoemission indicate the strong reduction of the oxidization state of the vanadium ion under oxygen deficiency. The estimated oxygen-vacancy level of the annealed sample $VO_{2-\delta}$ is $\delta = 0.08$ at 300 °C and $\delta = 0.2$ at 400 °C.

To further confirm that the metallic state is not a Magnéli phase and to study the stability of the metallic state at cryogenic temperatures, we measure the electrical resistivity of the 400-°C and 2-h annealed sample down to 1.8 K. Most Magnéli phases possess first-order metal-insulator transitions [46] and, thus, can be identified by the presence of abrupt resistivity jumps corresponding to their transition temperature T_{MIT} [46]. Figure 4(c) shows the cooling and heating resistivity curves of the annealed sample in the temperature region from 1.8 to 373 K. The transition temperatures of the Magnéli phases are also marked for comparison. Upon cooling to 1.8 K, no signature of a metal-insulator transition is observed in the annealed thin film. The combination of XRD and low-temperature transport studies, thus, demonstrates that the low-oxygen-pressure annealing primarily serves to introduce oxygen deficiency into VO_2 and stabilize the metallic rutile phase.

To study the level of oxygen deficiency in the metallized samples and its effect on the oxidation state of vanadium, XPS analysis is performed. Figure 4(d) shows the V2p core-level spectra of the pristine and annealed samples. For the pristine sample, the V2$p_{3/2}$ core-level photoemission peak mainly appears at 516.6 eV, close to the literature value of the V^{4+} valence state (515.5–516.4 eV) [26,38,47]. After annealing, the V2$p_{1/2}$ core-level photoemission peak shifts towards low binding energy, and the V2$p_{3/2}$ peak splits where a pronounced peak appears at lower binding energy, indicating the reduction of the vanadium ion after annealing. We confirm such a reduction behavior by measuring three different regions of the samples. The V2$p_{3/2}$ peak with lower binding energy (515.6 eV) corresponds to the V^{3+} valence state (515.1–515.8 eV) [26,38,47]. The oxygen nonstoichiometry of the $VO_{2-\delta}$ after annealing at low oxygen pressure is then estimated to be $\delta \sim 0.08$ at 300 °C and 0.2 at 400 °C by the ratio of the effective XPS peak area of V^{3+} and V^{4+} after the Shirley background is subtracted. It is reported that in electron-doped $V_{1-x}W_xO_2$ thin film, the phase transition is suppressed to approximately 50 K when $x \sim 0.09$ [48], where W takes the 6+ valence state [49]. Based on the charge neutrality ($V^{4+}_{1-3x}V^{3+}_{2x}W^{6+}_{x}O^{2-}_{2}$), about 0.197 electron doping per vanadium atom occurs. Assuming a similar amount of electron doping is required to suppress the phase transition in $VO_{2-\delta}$ ($V^{4+}_{1-2\delta}V^{3+}_{2\delta}O^{2-}_{2-\delta}$), the critical value of δ to suppress the phase transition is estimated to be 0.098 being consistent with present observations [Fig. 4(d)].

Previous work on phase equilibria in the V_2O_3-VO_2 system at 1600 K shows that the maximum concentration of oxygen vacancies in single-phase $VO_{2-\delta}$ is $\delta = 0.004$, beyond which Magnéli phases form [35]. It is, therefore, surprising that the oxygen-vacancy concentration generated by annealing can reach $\delta = 0.2$. We believe this is attributed to the extreme low oxygen partial pressure coupled with kinetic hindrance of structural degradation at the low annealing temperatures. Comparison to previous work reporting stabilization of the metallic state by electrolyte gating in a VO_2 field-effect transistor indicates that this level of oxygen deficiency can also be created by electric fields in electric double-layer transistors when the electrochemical stability window is exceeded [26,28]. Given the high levels of nonstoichiometry, such systems could be well suited for synchrotron studies to precisely investigate the local structure.

D. Destabilization on V—V dimerization in VO_2 due to oxygen vacancies

To further study the effect of oxygen vacancies on structural instability and V—V dimerization of VO_2 during the transition from its insulating monoclinic state to the

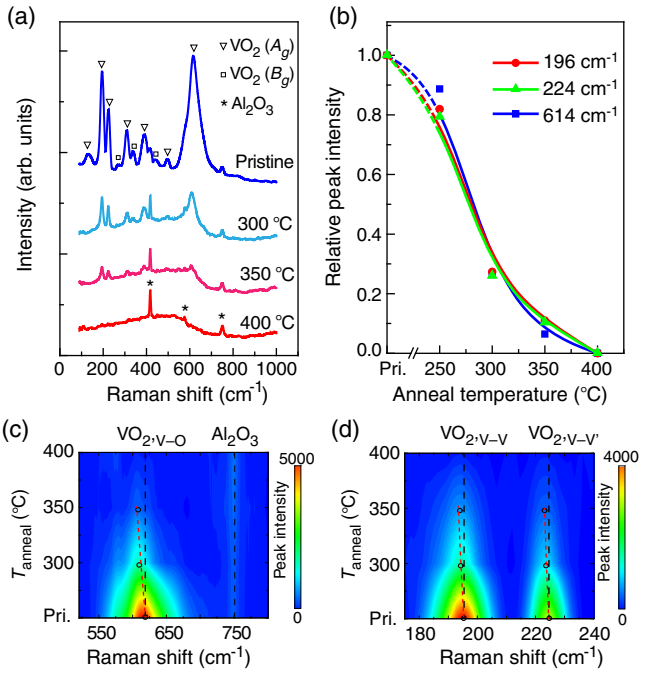

FIG. 5. Room-temperature Raman spectra of VO_2 after annealing at $P_{O_2} \sim 10^{-24}$ atm. (a) Raman spectra of PVD-grown 40-nm VO_2 annealed at 300 °C, 350 °C, and 400 °C for 2 h. For the pristine sample, Raman peaks corresponding to the monoclinic structure appear at 129, 196, 224, 308, 386, 498, and 614 cm^{-1} for A_g symmetry, and 268, 340, and 445 cm^{-1} for B_g symmetry. For the sample annealed at 400 °C, the heavily damped Raman peak at 530 cm^{-1} corresponds to the A_{1g} mode of the rutile structure. Peaks at 421, 575, and 751 cm^{-1} result from Raman scattering of the Al_2O_3 substrate. (b) Relative intensity of the Raman peaks at 196, 224, and 614 cm^{-1} as a function of the annealing temperature. (c) The A_g mode at 614 cm^{-1} as a function of the annealing temperature. This Raman mode is related to V—O bonding of VO_2. (d) The A_g modes at 196 and 224 cm^{-1} as a function of the annealing temperature. These Raman modes are related to V—V bonding and tilting of VO_2. Softening of the Raman modes, V—O bonding (c), and V—V bonding (d) occurs with the increase of the annealing temperature, demonstrating the instability of the monoclinic structure upon the introduction of oxygen vacancies.

oxygen-deficient metallic state, Raman spectra of PVD-grown 40-nm VO_2 annealed at 300 °C, 350 °C, and 400 °C for 2 h (i.e., increasing oxygen-vacancy concentration) are investigated. As Fig. 5(a) shows, the pristine VO_2 thin film is in the monoclinic structure at room temperature with sharp Raman peaks at 129, 196, 224, 308, 386, 498, and 614 cm^{-1} for A_g symmetry, and 268, 340, and 445 cm^{-1} for B_g symmetry [50,51]. Extra peaks at 421, 575, and 751 cm^{-1} are due to the Raman signal from the Al_2O_3 substrate. After annealing at 400 °C for 2 h, all peaks corresponding to the monoclinic structure vanish. Instead, a heavily damped Raman peak appears centered at 530 cm^{-1}. The value and shape of this damped peak are coincident with that of the A_{1g} mode of the thermally induced rutile metallic state in pristine VO_2 [50]. With increasing annealing temperature, the peak around 530 cm^{-1} corresponding to the rutile structure gradually becomes dominant, while the intensity of peaks corresponding to the monoclinic structure decreases [Fig. 5(b)], indicating the gradual reduction in the fraction of the insulating phase in the sample.

The shifting of Raman modes due to the introduction of oxygen vacancies is shown in Figs. 5(c) and 5(d). We focus on an A_g mode at 614 cm^{-1} related to V—O bonding [Fig. 5(c)] and A_g modes at 196 and 224 cm^{-1} related to the pairing and tilting of V—V bonds [Fig. 5(d)] [52,53]. After annealing at 400 °C for 2 h, the peak corresponding to the V—O bonding mode at 614 cm^{-1} [Fig. 5(c)] shifts down by 10 cm^{-1}. Simultaneously, the peaks corresponding to V—V dimerization at 196 and 224 cm^{-1} [Fig. 5(d)] shift down by 1.5 cm^{-1}. As a comparison, the Raman peak at 751 cm^{-1} from the substrate does not shift. The softening of the V—O and V—V mode is similar to that of the thermally induced metal-insulator transition in pristine VO_2 [52,54], indicating the destabilization of the monoclinic structure due to oxygen deficiency. Previous work indicates that the Peierls instability, i.e., distortion of the V—O octahedral and dimerization of V—V in the monoclinic state, plays an important role in opening an energy gap during the metal-insulator transition of VO_2 [11,14]. As a result, the emergence of the metallic state after low oxygen partial pressure annealing can be understood at least partially as the result of the degradation of the Peierls mechanism with respect to oxygen deficiency and reduction of V^{4+}.

E. Optical properties of the oxygen-deficient metallic state

The optical properties of the metallic state after annealing are further investigated by ellipsometry measurements. The refractive index data of a pristine PVD-grown 40-nm VO_2 film and one annealed at 400 °C for 2 h are presented in

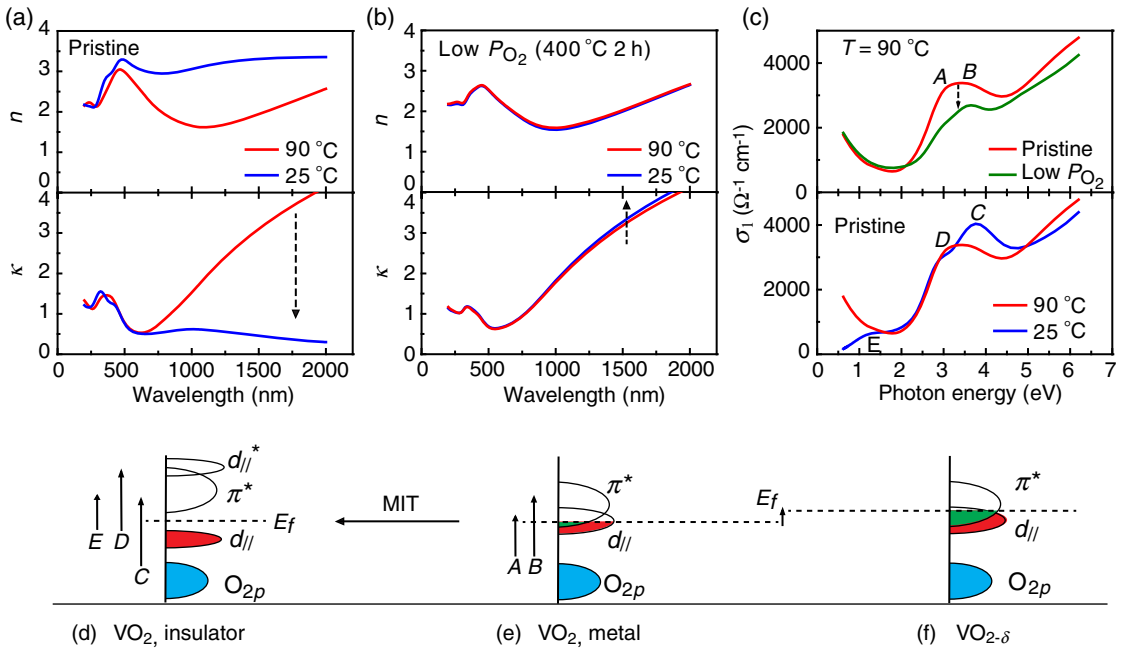

FIG. 6. Optical properties of VO_2 before and after annealing at $P_{O_2} \sim 10^{-24}$ atm. (a) Real (n) and imaginary (κ) parts of the complex refractive index of pristine VO_2 at 25 °C and 90 °C, below and above its metal-insulator-transition temperature. After annealing at $P_{O_2} \sim 10^{-24}$ atm, the complex refractive index of oxygen-deficient $VO_{2-\delta}$ at 25 °C and 90 °C is shown in (b), where Drude-like metallic behavior is observed and no phase transition occurs. (c) Comparison of the optical conductivity between the thermally induced metallic state of pristine VO_2 and the oxygen-deficiency-induced metallic state of $VO_{2-\delta}$ at 90 °C. The optical conductivity of pristine VO_2 across the thermally induced metal-insulator transition is shown in the lower panel. (d)–(f) Schematic illustration of the band structure of pristine VO_2 in the insulating state (d) and metallic state (e), while the band structure of oxygen-deficient $VO_{2-\delta}$ is shown in (f), where strong charge filling in the $\pi*$ and $d_{//}$ orbitals occurs.

Figs. 6(a) and 6(b). For pristine VO_2 [Fig. 6(a)], a large increase of the real part of refractive index n and a reduction in the extinction coefficient κ are observed in the wavelength range of 700–2000 nm across the metal- (90 °C) to-insulator (25 °C) transition [16]. Such a change is not seen in the annealed $VO_{2-\delta}$ film [Fig. 6(b)]. Moreover, the opposite temperature-dependent behavior occurs as the extinction coefficient κ of $VO_{2-\delta}$ increases slightly with cooling, demonstrating the vanishing of the metal-insulator transition that is consistent with electrical measurements [Fig. 2(a)]. The optical properties of $VO_{2-\delta}$ at both temperatures are found to be similar to that of pristine VO_2 at 90 °C, indicating that the metallized $VO_{2-\delta}$ is closely related to the thermally induced metallic state in pristine VO_2 [43]. The real part of the optical conductivity σ_1 of the oxygen-deficient sample is calculated from the complex refractive index and compared with the thermally induced metallic state in VO_2 [the upper panel of Fig. 6(c)] [43]. It is found that both samples show Drude-like behavior with similar optical conductivity in the low-photon-energy region.

Another interesting feature is the significant reduction of the broad absorption peak between 2.5 and 4 eV shown in the upper panel of Fig. 6(c). For a better understanding of this reduction, the band structure of VO_2 is depicted schematically in Figs. 6(d)–6(f) based on the Goodenough model [11]. In pristine metallic VO_2 [Fig. 6(e)], this absorption peak corresponds to the interband transitions from the O_{2p} band to the $\pi*$ and $d_{//}$ bands labeled as B and A, the energy value of which is consistent with previous works [55]. The $\pi*$ and $d_{//}$ bands are overlapped and partially filled in the metallic state. Upon the metal-insulator transition in pristine VO_2 [Fig. 6(d)], the $d_{//}$ band further splits due to the dimerization of vanadium ions and the $\pi*$ band shifts up, and an energy gap appears between the fully occupied lower $d_{//}$ band and the empty $\pi*$ band. Such band structure reconstruction is attributed to the combined effect of lattice-electron coupling (Peierls transition) and electron-electron correlations (Mott-Hubbard transition) [11,12,14–19]. The interband transition in the insulating state [Fig. 6(d)] gives rise to three peaks in its optical conductivity labeled as C, D, and E [Fig. 6(c) lower panel]. Under oxygen deficiency [Fig. 6(c) upper panel], the significant reduction of the two absorption peaks (A and B) compared to the metallic state of pristine VO_2 indicates the reduction of unoccupied states in the $\pi*$ and $d_{//}$ bands [Fig. 6(f)], i.e., band filling with electrons generated by the oxygen vacancies. Such a band-filling effect then suppresses the metal-insulator transition [4,20,22,32,36,56] and leads to the stabilization of the metallic state.

IV. CONCLUSIONS

We introduce an oxygen-gettering approach to create low oxygen partial pressures to study correlated electron materials. Our technique allows systematic postgrowth tuning of oxygen defects in a model system, VO_2, without introducing ionic liquids, water, or hydrogen, and without forming Magnéli phases. We show that the oxygen-deficiency level induced by this method can greatly exceed the solubility limit in equilibrium and can be used to reversibly modify the electrical, optical, and structural properties via a defect-induced nonvolatile metal-insulator transition. Disorder on the anion sublattice, which enables structural change and charge filling synergistically, is, therefore, an elegant approach to designing nonvolatile functional properties in correlated oxides. Such materials with widely adaptive properties and environmental response hold promise in neuromorphic computing and adaptive electromagnetics.

ACKNOWLEDGMENTS

Funding from the Army Research Office and Office of Naval Research is acknowledged. This work is partially financed by the Initiative and Networking Fund of the German Helmholtz Association, Helmholtz Virtual Institute Grant No. VH-VI-422 MEMRIOX. M. A. K. acknowledges support from the Office of Naval Research (Grant No. N00014-16-1-2556). V. S. and A. B. acknowledge support from the Air Force Office of Scientific Research MURI Grant No. FA9550-14-1-0389. H. H. P. receives support from an American Society for Engineering Education Fellowship; T. L. receives support from National Research Council Fellowship.

APPENDIX A: Mg-BASED OXYGEN-TRAP SYSTEM DESIGN AND OPERATING PRINCIPLE

Figure 7 shows a cross-sectional schematic of the Mg-based O_2-trap setup built for our study. Mg powder (Sigma Aldrich) is placed between ceramic insulation rolls inside a stainless-steel tube container. The stainless-steel tube is wrapped by a heating tape powered by a variable transformer (Staco Energy), and the temperature near the working zone of the O_2 trap is monitored by a thermocouple. A layer of ceramic insulation roll covers the heating tape and the stainless-steel tube container to reduce heat

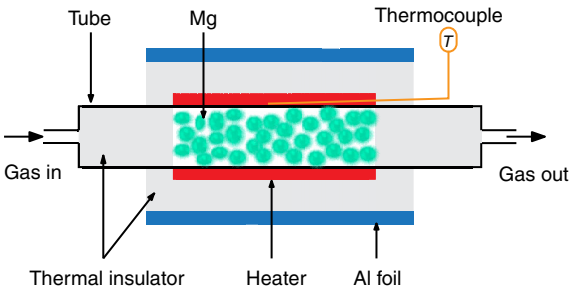

FIG. 7. Schematic of the Mg-based oxygen trap for achieving ultralow oxygen partial pressure.

TABLE I. Calculated equilibrium constant (K_{eq}) of $2Mg + O_2(g) = 2MgO$.

Temperature (°C)	K_{eq}
350	3.83×10^{89}
400	1.26×10^{82}
450	4.49×10^{75}
500	1.10×10^{70}

dissipation during heating. A piece of aluminum foil sheaths the porous ceramic insulation roll.

When Ar gas flows into the oxygen-trap setup, the trace amount of O_2 impurity reacts with the Mg following the reaction: $2Mg + O_2(g) = 2MgO$. The MgO formed is porous and, thus, does not prevent further reaction from taking place. The theoretical P_{O_2} at the Mg/MgO equilibrium can be calculated from the equilibrium constant (K_{eq}) of the reaction following the equation: $P_{O_2} = a_{MgO^2}/(a_{Mg^2} \cdot K_{eq})$, where $a_{MgO} = 1$ is the activity of MgO, and $a_{Mg} = 1$ is the activity of Mg. The value of K_{eq} as a function of temperature from 350 °C to 500 °C is obtained from the HSC Chemistry Database [57] and shown in Table I. In addition to thermodynamic considerations, the actual P_{O_2} in the Ar gas after passing through the Mg-based O_2-trap setup is strongly influenced by the kinetic factors including the reaction rate and time. Although the equilibrium P_{O_2} goes down as the operation temperature decreases, the reaction rate also decreases. Therefore, the operation temperature cannot be too low and sets experimental limits. The optimum operation temperature of the Mg-based O_2 trap is typically a few hundred degrees to ensure both a low equilibrium P_{O_2} and a relatively high reaction rate. In this work, we heat the Mg to 450 °C, which enables a theoretical oxygen partial pressure of about 10^{-75} atm. In experiments, the theoretical oxygen partial pressure is difficult to reach due to the constant flowing of Ar gas and the possible gas leakage near the tube fitting area. As shown in Fig. 1(b), an oxygen partial pressure as low as 10^{-24} atm is reached in our work. In future experiments, if we can control the flow rate to lower values, it is possible to achieve even lower partial pressures. For instance, Chiang and co-workers [58] have demonstrated similar solid-state buffering routes to reach 10^{-40}-atm oxygen partial pressures in studies of the stability of Si-SiO_2 interfaces.

At very low partial pressure, the kinetics of oxygen molecules becomes relevant. Based on the kinetic theory of gases, the impingement rate Z, i.e., the number of molecules striking the surface perpendicular to their moving direction, per unit time, is expressed as [59]

$$Z = \frac{P}{\sqrt{2\pi m k_B T}} = 8.333 \times 10^{22} P/(TM)^{\frac{1}{2}} \quad (\text{molecules/m}^2\,\text{s}), \tag{A1}$$

where P is the pressure of gas (Pa), T is the temperature (K), m is mass of gas molecules (g), M is molar mass (kg/mol), and k_B is the Boltzmann constant. In our experiment, the surface area of the oxygen sensor is about 4×10^{-4} m^2. The impingement rate is about one molecule per 10 s at oxygen partial pressure of approximately 10^{-25} atm. In comparison, at ambient condition, the impingement rate is approximately 10^{23} molecules/s. The slow kinetics of oxygen molecules drives the system away from thermodynamic equilibrium state. In experiment, however, the oxygen sensor continuously monitors the oxygen partial pressure inside the annealing system and assumes thermodynamic equilibrium is achieved. Thus, the oxygen partial pressure measured by the oxygen sensor effectively represents the local near-surface and nonequilibrium value of P_{O_2}. Because a similar environment is experienced by both the oxygen sensor and vanadium dioxide samples, we use such an effective value to characterize the low oxygen partial pressure environment near the sample surface.

APPENDIX B: ZIRCONIA-BASED OXYGEN SENSOR

Zirconia-based oxygen sensors are widely used for determining P_{O_2} in a test gas at high temperatures as well as in automotive exhaust systems. The most common application is to measure the P_{O_2} in exhaust gas in order to maintain an optimized air-to-fuel ratio [60]. The literature also shows that this type of oxygen sensor is capable of measuring a P_{O_2} as low as approximately 10^{-35} atm in an oxygen-poor gas environment [61].

Figure 8 shows a schematic of the zirconia-based oxygen sensor. The zirconia-based oxygen sensor is a potentiometric sensor. It consists of a tubular oxygen-ion-conducting zirconia electrolyte and porous Pt anode and cathode. It is typically operated at a high temperature in the range of 500 °C to 800 °C to facilitate the chemical and electrochemical processes involved. In our work, the inside of the zirconia tube is exposed to air with a constant $P_{O_2(air)}$ of 0.21 atm,

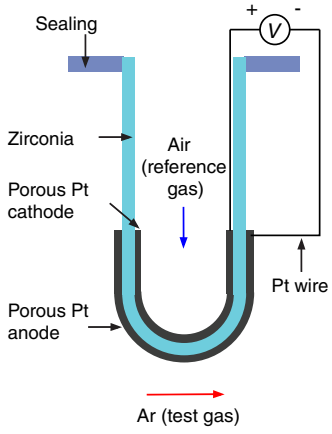

FIG. 8. Schematic of the zirconia-based oxygen sensor.

while the outside to the test gas that has a much lower $P_{O_2(Ar)}$. The same chemical species (oxygen) is present at both electrodes but at different partial pressures. Therefore, this oxygen sensor device is regarded as a concentration cell. Because of the difference in the oxygen partial pressure between the air outside the chamber and Ar inside the chamber, the cell develops a voltage, which can be expressed as follows according to the Nernst equation [62,63]:

$$E = \frac{RT}{4F}\ln\left(\frac{a_{O_2(YSZ-Pt\text{-}air)}}{a_{O_2(YSZ-Pt\text{-}Ar)}}\right), \tag{B1}$$

where E is the Nernst potential, R is the gas constant (8.31 J mol^{-1} K^{-1}), T is the operating temperature of the oxygen sensor (550 °C here), F is the Faraday constant (96 485 C mol^{-1}), $a_{O_2(YSZ-Pt\text{-}air)}$ is the oxygen activity at the triple phase boundary between YSZ (yttria-stabilized zirconia), Pt cathode, and air, and $a_{O_2(YSZ-Pt\text{-}Ar)}$ is the oxygen activity at the triple phase boundary between the YSZ, Pt anode, and Ar. Under thermodynamic equilibrium condition, the oxygen activity at the YSZ-Pt-gas triple phase boundary equals the oxygen activity in the gas, which is expressed as the oxygen partial pressure in the gas divided by the standard pressure (1 atm). Therefore, the Nernst potential can be expressed as

$$E = \frac{RT}{4F}\ln\left(\frac{P_{O_2(air)}}{P_{O_2(Ar)}}\right), \tag{B2}$$

where $P_{O_2(air)}$ is the oxygen partial pressure in air (0.21 atm), and $P_{O_2(Ar)}$ is the oxygen partial pressure of Ar inside the annealing system. By measuring the Nernst potential, the oxygen partial pressure inside the annealing system can be calculated by Eq. (B2).

In experiment, the Nernst relation is valid and enables us to measure the oxygen partial pressure inside the annealing system when the ionic conductivity is dominant over electronic conductivity for zirconia electrolyte, thus, determining its dynamic range. For a typical zirconia electrolyte (8-mole-% yttria-stabilized zirconia), the ion, electron, and hole conductivities at 800 °C–1050 °C and P_{O_2} (0.21–10^{-17} atm) in Ω^{-1} cm^{-1} are reported as [64]

$$\sigma_{ion} = 1.63\times10^{2}\exp\left(-0.79\ \frac{eV}{kT}\right), \tag{B3}$$

$$\sigma_{e} = 1.31\times10^{7}\exp\left(-3.88\ \frac{eV}{kT}\right)P_{O_2}^{-1/4}, \tag{B4}$$

$$\sigma_{h} = 2.35\times10^{2}\exp\left(-1.67\ \frac{eV}{kT}\right)P_{O_2}^{+1/4}. \tag{B5}$$

Based on these relations, the ion, electron, and hole conductivities are calculated and shown in Fig. 9. With the extrapolation of these relations in our measurement range (550 °C and 0.21–10^{-24} atm), the estimated ionic conductivity is more than 3 orders of magnitude higher than electron conductivity. This extrapolation to lower temperature is valid for zirconia since the electron contribution becomes less relevant with reducing temperature [64]. In addition, such a calculated result is also consistent with the reported experimental observations that the ionic conduction is dominant over the 10^{-24}-atm partial pressure range in stabilized zirconia [65]. Thus, in this work, we still work within the dynamic range of zirconia-based oxygen sensors.

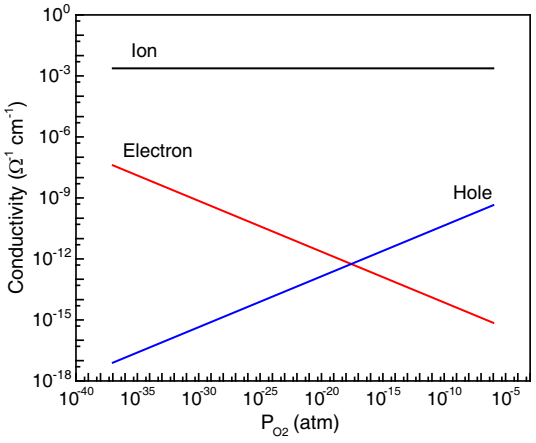

FIG. 9. Ion, electron, and hole conductivity of zirconia at 550 °C calculated based on Eqs. (B3)–(B5).

In this work, we measure the Nernst potential with a Solartron 1287 electrochemical system, which provides a resolution of 10^{-5} V. The experimental Nernst potential (raw data) recorded during annealing is shown in Fig. 10. The noise on the recorded Nernst potential results from the fluctuation of local oxygen pressure near the sensor surface and the noise from the sensor and measurement system.

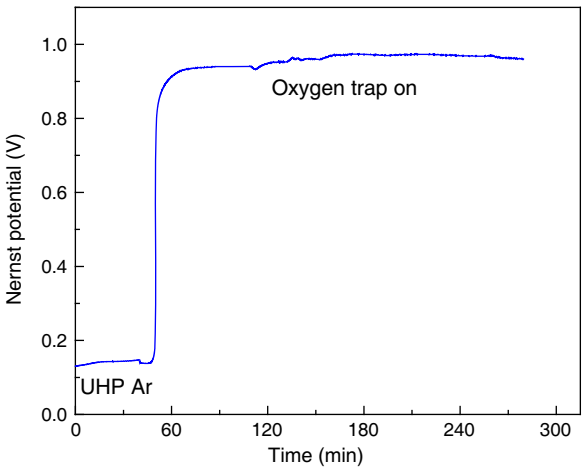

FIG. 10. The experimental Nernst potential measured during low oxygen partial pressure annealing.

It can be found in Fig. 10 that when the Mg-based trap is turned on, the Nernst potential increases from approximately 0.1 V to approximately 0.95 V. Such an increase in the Nernst potential is much larger than the noise of the signals, which, therefore, ensures the reliability of our measurement.

[1] S. V. Kalinin and N. A. Spaldin, Functional ion defects in transition metal oxides, Science **341**, 858 (2013).

[2] C. Wu, F. Feng, and Y. Xie, Design of vanadium oxide structures with controllable electrical properties for energy applications, Chem. Soc. Rev. **42**, 5157 (2013).

[3] J. Shi, Y. Zhou, and S. Ramanathan, Colossal resistance switching and band gap modulation in a perovskite nickelate by electron doping, Nat. Commun. **5**, 4860 (2014).

[4] K. Holman, T. McQueen, A. Williams, T. Klimczuk, P. Stephens, H. Zandbergen, Q. Xu, F. Ronning, and R. Cava, Insulator to correlated metal transition in $V_{1-x}Mo_xO_2$, Phys. Rev. B **79**, 245114 (2009).

[5] M. Marezio, D. B. McWhan, J. Remeika, and P. Dernier, Structural aspects of the metal-insulator transitions in Cr-doped VO_2, Phys. Rev. B **5**, 2541 (1972).

[6] C. Tang, P. Georgopoulos, M. Fine, J. Cohen, M. Nygren, G. Knapp, and A. Aldred, Local atomic and electronic arrangements in $W_xV_{1-x}O_2$, Phys. Rev. B **31**, 1000 (1985).

[7] Z. Yang, C. Ko, and S. Ramanathan, Oxide electronics utilizing ultrafast metal-insulator transitions, Annu. Rev. Mater. Res. **41**, 337 (2011).

[8] J. Rensberg, S. Zhang, Y. Zhou, A. S. McLeod, C. Schwarz, M. Goldflam, M. Liu, J. Kerbusch, R. Nawrodt, S. Ramanathan, D. N. Basov, F. Capasso, C. Ronning, and M. A. Kats, Active optical metasurfaces based on defect-engineered phase-transition materials, Nano Lett. **16**, 1050 (2016).

[9] M. A. Kats, R. Blanchard, S. Zhang, P. Genevet, C. Ko, S. Ramanathan, and F. Capasso, Vanadium Dioxide as a Natural Disordered Metamaterial: Perfect Thermal Emission and Large Broadband Negative Differential Thermal Emittance, Phys. Rev. X **3**, 041004 (2013).

[10] T. Paik, S.-H. Hong, E. A. Gaulding, H. Caglayan, T. R. Gordon, N. Engheta, C. R. Kagan, and C. B. Murray, Solution-processed phase-change VO_2 metamaterials from colloidal vanadium oxide (VO_x) nanocrystals, ACS Nano **8**, 797 (2014).

[11] J. B. Goodenough, The two components of the crystallographic transition in VO_2, J. Solid State Chem. **3**, 490 (1971).

[12] R. M. Wentzcovitch, W. W. Schulz, and P. B. Allen, VO_2: Peierls or Mott-Hubbard? A View from Band Theory, Phys. Rev. Lett. **72**, 3389 (1994).

[13] F. J. Morin, Oxides Which Show a Metal-to-Insulator Transition at the Neel Temperature, Phys. Rev. Lett. **3**, 34 (1959).

[14] C. Weber, D. D. O'Regan, N. D. Hine, M. C. Payne, G. Kotliar, and P. B. Littlewood, Vanadium Dioxide: A Peierls-Mott Insulator Stable against Disorder, Phys. Rev. Lett. **108**, 256402 (2012).

[15] A. Zylbersztejn and N. F. Mott, Metal-insulator transition in vanadium dioxide, Phys. Rev. B **11**, 4383 (1975).

[16] M. M. Qazilbash, M. Brehm, B.-G. Chae, P.-C. Ho, G. O. Andreev, B.-J. Kim, S. J. Yun, A. V. Balatsky, M. B. Maple, F. Keilmann, H.-T. Kim, and D. N. Basov, Mott transition in VO_2 revealed by infrared spectroscopy and nano-imaging, Science **318**, 1750 (2007).

[17] M. Abbate, F. De Groot, J. Fuggle, Y. Ma, C. Chen, F. Sette, A. Fujimori, Y. Ueda, and K. Kosuge, Soft-x-ray-absorption studies of the electronic-structure changes through the VO_2 phase transition, Phys. Rev. B **43**, 7263 (1991).

[18] S. Biermann, A. Poteryaev, A. Lichtenstein, and A. Georges, Dynamical Singlets and Correlation-Assisted Peierls Transition in VO_2, Phys. Rev. Lett. **94**, 026404 (2005).

[19] M. Haverkort, Z. Hu, A. Tanaka, W. Reichelt, S. Streltsov, M. Korotin, V. Anisimov, H. Hsieh, H.-J. Lin, and C. Chen, Orbital-Assisted Metal-Insulator Transition in VO_2, Phys. Rev. Lett. **95**, 196404 (2005).

[20] J. Wei, H. Ji, W. Guo, A. H. Nevidomskyy, and D. Natelson, Hydrogen stabilization of metallic vanadium dioxide in single-crystal nanobeams, Nat. Nanotechnol. **7**, 357 (2012).

[21] N. B. Aetukuri, A. X. Gray, M. Drouard, M. Cossale, L. Gao, A. H. Reid, R. Kukreja, H. Ohldag, C. A. Jenkins, and E. Arenholz, Control of the metal-insulator transition in vanadium dioxide by modifying orbital occupancy, Nat. Phys. **9**, 661 (2013).

[22] M. Imada, A. Fujimori, and Y. Tokura, Metal-insulator transitions, Rev. Mod. Phys. **70**, 1039 (1998).

[23] J. G. Ramirez, T. Saerbeck, S. Wang, J. Trastoy, M. Malnou, J. Lesueur, J.-P. Crocombette, J. E. Villegas, and I. K. Schuller, Effect of disorder on the metal-insulator transition of vanadium oxides: Local versus global effects, Phys. Rev. B **91**, 205123 (2015).

[24] V. Andreev, V. Klimov, and M. Kompan, Influence of hydrogenation on electrical conductivity of vanadium dioxide thin films, Phys. Solid State **54**, 601 (2012).

[25] Z. Yang, Y. Zhou, and S. Ramanathan, Studies on room-temperature electric-field effect in ionic-liquid gated VO_2 three-terminal devices, J. Appl. Phys. **111**, 014506 (2012).

[26] J. Jeong, N. Aetukuri, T. Graf, T. D. Schladt, M. G. Samant, and S. S. Parkin, Suppression of metal-insulator transition in VO_2 by electric field-induced oxygen vacancy formation, Science **339**, 1402 (2013).

[27] M. Nakano, K. Shibuya, D. Okuyama, T. Hatano, S. Ono, M. Kawasaki, Y. Iwasa, and Y. Tokura, Collective bulk carrier delocalization driven by electrostatic surface charge accumulation, Nature (London) **487**, 459 (2012).

[28] Y. Zhou and S. Ramanathan, Relaxation dynamics of ionic liquid—VO_2 interfaces and influence in electric double-layer transistors, J. Appl. Phys. **111**, 084508 (2012).

[29] H. Ji, J. Wei, and D. Natelson, Modulation of the electrical properties of VO_2 nanobeams using an ionic liquid as a gating medium, Nano Lett. **12**, 2988 (2012).

[30] X. Peng, Y. Yang, Y. Hou, H. C. Travaglini, L. Hellwig, S. Hihath, K. van Benthem, K. Lee, W. Liu, and D. Yu, Efficient and Hysteresis-Free Field Effect Modulation of Ambipolarly Doped Vanadium Dioxide Nanowires, Phys. Rev. Applied **5**, 054008 (2016).

[31] M. Goldflam, M. Liu, B. Chapler, H. Stinson, A. Sternbach, A. McLeod, J. Zhang, K. Geng, M. Royal, and B.-J. Kim, Voltage switching of a VO_2 memory metasurface using ionic gel, Appl. Phys. Lett. **105**, 041117 (2014).
[32] C. Griffiths and H. Eastwood, Influence of stoichiometry on the metal-semiconductor transition in vanadium dioxide, J. Appl. Phys. **45**, 2201 (1974).
[33] H.-T. Zhang, L. Zhang, D. Mukherjee, Y.-X. Zheng, R. C. Haislmaier, N. Alem, and R. Engel-Herbert, Wafer-scale growth of VO_2 thin films using a combinatorial approach, Nat. Commun. **6**, 8475 (2015).
[34] D. Ruzmetov, S. D. Senanayake, V. Narayanamurti, and S. Ramanathan, Correlation between metal-insulator transition characteristics and electronic structure changes in vanadium oxide thin films, Phys. Rev. B **77**, 195442 (2008).
[35] T. Katsura and M. Hasegawa, Equilibria in the V_2O_3—VO_2 system at 1600° K, Bull. Chem. Soc. Jpn. **40**, 561 (1967).
[36] S. Zhang, I. S. Kim, and L. J. Lauhon, Stoichiometry engineering of monoclinic to rutile phase transition in suspended single crystalline vanadium dioxide nanobeams, Nano Lett. **11**, 1443 (2011).
[37] See Supplemental Material at http://link.aps.org/supplemental/10.1103/PhysRevApplied.7.034008 for the thermodynamic analysis of the stability of vanadium dioxide and sapphire substrate at low oxygen partial pressures, ellipsometry data, and model fitting of vanadium dioxide after annealing, annealing of 100-nm PVD-grown vanadium dioxide film at low oxygen partial pressure, stability of vanadium dioxide after annealing at ambient condition, annealing of vanadium dioxide at low oxygen partial pressure over multiple cycles, and off-axis XRD studies of vanadium dioxide after annealing.
[38] E. Hryha, E. Rutqvist, and L. Nyborg, Stoichiometric vanadium oxides studied by XPS, Surf. Interface Anal. **44**, 1022 (2012).
[39] D. D. S. Meneses, M. Malki, and P. Echegut, Structure and lattice dynamics of binary lead silicate glasses investigated by infrared spectroscopy, J. Non-Cryst. Solids **352**, 769 (2006).
[40] T. E. Tiwald, D. W. Thompson, J. A. Woollam, W. Paulson, and R. Hance, Application of IR variable angle spectroscopic ellipsometry to the determination of free carrier concentration depth profiles, Thin Solid Films **313**, 661 (1998).
[41] J. Wei, Z. Wang, W. Chen, and D. H. Cobden, New aspects of the metal-insulator transition in single-domain vanadium dioxide nanobeams, Nat. Nanotechnol. **4**, 420 (2009).
[42] F. Gervais and B. Piriou, Anharmonicity in several-polar-mode crystals: Adjusting phonon self-energy of LO and TO modes in Al_2O_3 and TiO_2 to fit infrared reflectivity, J. Phys. C **7**, 2374 (1974).
[43] M. Qazilbash, K. Burch, D. Whisler, D. Shrekenhamer, B. Chae, H. Kim, and D. Basov, Correlated metallic state of vanadium dioxide, Phys. Rev. B **74**, 205118 (2006).
[44] F. J. Wong, Y. Zhou, and S. Ramanathan, Epitaxial variants of VO_2 thin films on complex oxide single crystal substrates with 3*m* surface symmetry, J. Cryst. Growth **364**, 74 (2013).
[45] K. Rogers, An x-ray diffraction study of semiconductor and metallic vanadium dioxide, Powder Diffr. **8**, 240 (1993).
[46] S. Kachi, K. Kosuge, and H. Okinaka, Metal-insulator transition in V_nO_{2n-1}, J. Solid State Chem. **6**, 258 (1973).
[47] G. Silversmit, D. Depla, H. Poelman, G. B. Marin, and R. De Gryse, Determination of the V2p XPS binding energies for different vanadium oxidation states (V^{5+} to V^{0+}), J. Electron Spectrosc. Relat. Phenom. **135**, 167 (2004).
[48] K. Shibuya, M. Kawasaki, and Y. Tokura, Metal-insulator transition in epitaxial $V_{1-x}W_xO_2$ ($0 \leq x \leq 0.33$) thin films, Appl. Phys. Lett. **96**, 022102 (2010).
[49] H. Takami, T. Kanki, S. Ueda, K. Kobayashi, and H. Tanaka, Electronic structure of W-doped VO_2 thin films with giant metal–insulator transition investigated by hard x-ray core-level photoemission spectroscopy, Appl. Phys. Express **3**, 063201 (2010).
[50] R. Srivastava and L. Chase, Raman Spectrum of Semiconducting and Metallic VO_2, Phys. Rev. Lett. **27**, 727 (1971).
[51] P. Schilbe and D. Maurer, Lattice dynamics in VO_2 near the metal-insulator transition, Mater. Sci. Eng. A **370**, 449 (2004).
[52] H.-T. Kim, B.-G. Chae, D.-H. Youn, G. Kim, K.-Y. Kang, S.-J. Lee, K. Kim, and Y.-S. Lim, Raman study of electric-field-induced first-order metal-insulator transition in VO_2-based devices, Appl. Phys. Lett. **86**, 242101 (2005).
[53] J. M. Atkin, S. Berweger, E. K. Chavez, M. B. Raschke, J. Cao, W. Fan, and J. Wu, Strain and temperature dependence of the insulating phases of VO_2 near the metal-insulator transition, Phys. Rev. B **85**, 020101 (2012).
[54] J. D. Budai, J. Hong, M. E. Manley, E. D. Specht, C. W. Li, J. Z. Tischler, D. L. Abernathy, A. H. Said, B. M. Leu, and L. A. Boatner, Metallization of vanadium dioxide driven by large phonon entropy, Nature (London) **515**, 535 (2014).
[55] M. M. Qazilbash, A. Schafgans, K. Burch, S. Yun, B. Chae, B. Kim, H.-T. Kim, and D. Basov, Electrodynamics of the vanadium oxides VO_2 and V_2O_3, Phys. Rev. B **77**, 115121 (2008).
[56] A. Cavalleri, M. Rini, H. Chong, S. Fourmaux, T. Glover, P. Heimann, J. Kieffer, and R. Schoenlein, Band-Selective Measurements of Electron Dynamics in VO_2 Using Femtosecond Near-Edge X-Ray Absorption, Phys. Rev. Lett. **95**, 067405 (2005).
[57] A. Roine, *HSC Chemistry Database 5.11* (Outokumpu Research, Finland, 2002).
[58] E. Jud, M. Tang, and Y.-M. Chiang, Stability of $HfO_2/SiO_x/Si$ surficial films at ultralow oxygen activity, J. Appl. Phys. **103**, 114108 (2008).
[59] A. Chambers, *Modern Vacuum Physics* (Chapman & Hall/CRC, Boca Raton, FL, 2004).
[60] R. Ramamoorthy, P. Dutta, and S. Akbar, Oxygen sensors: Materials, methods, designs and applications, J. Mater. Sci. **38**, 4271 (2003).
[61] A. Inoishi, Y.-W. Ju, S. Ida, and T. Ishihara, Mg–air oxygen shuttle batteries using a ZrO_2-based oxide ion-conducting electrolyte, Chem. Commun. (Cambridge) **49**, 4691 (2013).
[62] A. J. Bard and L. Faulkner, *Electrochemical Methods: Principles and Applications*, 2nd ed. (Wiley New York, 2001).
[63] R. O'hayre, S.-W. Cha, F. B. Prinz, and W. Colella, *Fuel Cell Fundamentals* (John Wiley & Sons, New York, 2016).
[64] J. H. Park and R. N. Blumenthal, Electronic transport in 8 mole percent $Y_2O_3 - ZrO_2$, J. Electrochem. Soc. **136**, 2867 (1989).
[65] N. Q. Minh, Ceramic fuel cells, J. Am. Ceram. Soc. **76**, 563 (1993).